Spatio-temporal approach to moving window block kriging of satellite data

Jovan M. Tadić[1], Xuemei Qiu[1], Scot Miller[1] and Anna M. Michalak[1]

[1]{Department of Global Ecology, Carnegie Institution for Science, Stanford, CA 94305, USA}

Abstract. Numerous existing satellites observe physical or environmental properties of the Earth system. Many of these satellites provide global-scale observations, but these observations are often sparse and noisy. By contrast, contiguous, global maps are often most useful to the scientific community (i.e., level 3 products). We develop a spatiotemporal moving window block kriging method to create contiguous maps from sparse and/or noisy satellite observations. This approach exhibits several advantages over existing methods: 1) it allows for flexibility in setting the spatial resolution of the level 3 map, 2) it is applicable to observations with variable density, 3) it produces a rigorous uncertainty estimate, 4) it exploits both spatial and temporal correlations in the data, and 5) it facilitates estimation in real time. Moreover, this approach only requires the assumption that the observable quantity exhibits spatial and temporal correlations that are inferable from the data. We test this method by creating Level 3 products from satellite observations of CO_2 (XCO_2) from the Greenhouse Gases Observing Satellite (GOSAT), CH_4 (XCH_4) from the Infrared Atmospheric Sounding Interferometer (IASI) and solar-induced chlorophyll fluorescence (SIF) from the Global Ozone Monitoring Experiment–2 (GOME-2). We evaluate and analyze the difference in performance of spatio-temporal vs. recently developed spatial kriging methods.

1. Introduction

Satellite observations of the Earth's surface and atmosphere provide a valuable window into the functioning of the Earth system. Satellites often provide global observations, but these observations are rarely uniform or contiguous in space/time. The observations can be non-contiguous due to satellite orbit geometries and periods, geophysical limitations (e.g. cloud cover), and temporary instrument malfunctions. Furthermore, satellites may provide a large quantity of data, but individual observations can have a large noise-to-signal ratio. It is often necessary to spatially interpolate the data in order to organize the data onto a regular grid, query the data at a particular location of interest, estimate data at unsampled times and/or locations, and/or map the underlying signal in a noisy dataset. These gridded, interpolated maps are commonly named "Level 3" data (e.g. NASA, 2014) and are often part of the standard suite of satellite data products.

CO_2 column observations (XCO_2) from the Greenhouse Gases Observing Satellite (GOSAT), CH_4 column observations (XCH_4) from the Infrared Atmospheric Sounding Interferometer (IASI) and solar-induced chlorophyll fluorescence (SIF) observations from The Global Ozone Monitoring Experiment–2 (GOME-2) provide prototypical examples of these challenges, and these three satellites are the primary application used throughout this work (see Section 3).

The most commonly-used method for creating Level 3 maps from satellite data is binning. This approach involves taking the mean of all observations within a given grid cell or "bin" (see Kulawik et al., 2010, and Crévoisier et al., 2009 for examples). The binning method, however, has a number of shortfalls that can lead to inconsistent or inaccurate results. First, different bins contain variable numbers of observations. As a result, some bins will be well-constrained by the data while others may be based upon sparse, noisy

41 observations. Second, binning does not produce uncertainty estimates. Third, this method cannot
42 extrapolate the unknown quantity to bins without any observations.

43 A broad class of geostatistical methods known as kriging provides an alternative approach to mapping
44 satellite observations. Kriging is a best linear unbiased estimator (for kriging see Chiles and Delfiner, 2012),
45 where covariance functions are used to represent correlations among data. As a result, kriging can account
46 for a variable density of observations and can estimate uncertainties in the resulting maps. Various forms
47 of kriging have recently been used to map satellite Earth observations, particularly for XCO_2 (e.g.,
48 Hammerling et al. 2012a,b; Tadić et al., 2015; Zeng et al., 2013; Guo et al., 2013, Zeng et al., 2016).
49 Hammerling et al. (2012a,b) presented an approach to map Orbiting Carbon Observatory-2 (OCO-2) and
50 GOSAT XCO_2 observations, respectively, with non-stationary properties. In our previous study (Tadić et
51 al., 2015) we extended that approach to create XCO_2 maps that can have a different spatial resolution from
52 the resolution or footprint of the original satellite observations. Our previous study and those of
53 Hammerling et al. (2012a,b) accounted for spatial covariances among observations but did not include a
54 temporal component. The present study extends this geostatistical framework from a purely spatial to a
55 spatiotemporal domain.

56 Spatiotemporal approaches to interpolation can provide a number of advantages relative to purely spatial
57 methods (e.g. Zeng et al., 2016; Guo et al., 2013). A purely spatial approach will usually aggregate
58 observations into temporal blocks; observations within the same block effectively have the same time stamp
59 whether or not those observations are actually synchronous (e.g., Tadić et al., 2015; Hammerling et al.,
60 2012a,b). Any real temporal variability within a block becomes noise. A spatiotemporal approach, by
61 contrast, treats time as an explicit dimension and models covariances among data as a function of time.

62 A handful of recent studies have considered temporal relationships when mapping satellite observations of
63 XCO_2. These studies have either used various forms of Kalman smoothing (e.g., Katzfuss and Cressie 2011,
64 Katzfuss and Cressie 2012, Nguyen et al. 2014) or geostatistics (e.g., Guo et al. 2013; Zeng et al. 2013;
65 Zeng et al. 2016). The former group of studies leverages Kalman smoothing to improve the computational
66 tractability of mapping dense or abundant datasets, like OCO-2 and the Atmospheric Infrared Sounder
67 (AIRS). The latter group of studies, by contrast, has applied geostatistics to sparse datasets like those from
68 the GOSAT satellite. A detailed review of spatial and spatio-temporal mapping methods has been published
69 recently (Li and Heap, 2014).

70 The goal of this study is to develop a geostatistical spatio-temporal mapping and upscaling method
71 (applicable, but not limited to, satellite observations of XCO_2) that exhibits several advances relative to
72 previous methods. It can: (1) fill in temporal gaps in the observations, (2) create maps at higher temporal
73 resolutions than purely spatial approach, (3) produce more accurate estimates when observations have
74 variable spatio-temporal coverage, (4) predict future values (i.e. extrapolate temporally). Among other
75 improvements, we develop an efficient method for subsampling satellite observations and utilize the
76 product-sum covariance model (e.g., De Iaco et al., 2001) that is easy to parameterize, which makes it
77 applicable to both dense and sparse datasets. The entire work has been conducted in Matlab 2012a.

78 Section 2 of this study describes the presented model in detail; it describes an efficient subsampling
79 procedure that can handle very large datasets and a covariance model that can estimate both spatial and
80 temporal relationships in the data. We then incorporate these components into a spatiotemporal version of
81 moving window block kriging. In sections 3 and 4, we subsequently apply this model to map GOSAT
82 XCO_2, IASI XCH_4 and GOME-2 SIF at multiple time resolutions (including daily).

2. Methods

The spatio-temporal block kriging approach presented in this study proceeds in three steps for each model grid cell and estimation time. First, we subsample the observations within a predetermined spatio-temporal domain (section 2.1). Next, we characterize the local spatio-temporal covariance structure (section 2.2). Finally, we interpolate the satellite observations at the desired spatial resolution (section 2.3).

2.1 Subsampling of observations

The ultimate goal of the proposed subsampling strategy is to reduce the number of observations in the spatio-temporal vicinity of an estimation location to a representative, computationally feasible subset of data. We use a subset of observations (M) to estimate a local set of covariance parameters and use another subset (N) to estimate the desired quantity and associated uncertainty. Note that, for the method presented here, M and N can refer to either the same subset of data or different subsets.

The total number of observations used for covariance parameter estimation (M), is selected to be small enough to make this estimation computationally feasible but large enough to yield a sample representative of both local and regional variability. The optimal subset of N observations used for mapping depends on the actually observed covariance structure which is not known prior to covariance parametrization step. In the example presented in Sect. 3, the optimal observational subset used in a mapping step for each grid cell comprised N points having the highest covariance with the estimation location. In the example below, we set both M and N at 500; larger values of M and N did not have a substantial impact on the estimated parameters and mapped quantity, respectively.

We select subset of observations M for each estimation grid cell by assigning a relative selection probability to each observation based on that observation's spatial and temporal 'separation distances' from the centroid of the grid cell. In the absence of a proper metric for distance in space-time, we model the spatial and temporal components of the overall selection probability separately.

The selection probability (and its components) is described by the following equation:

$$P = P_s \times P_t \propto 1/(A_s h_s)^2 \times e^{-(A_t h_t)^2} \tag{1}$$

where P_s is the spatial component of the relative probability of a given observation being selected, P_t is temporal component, h_s and h_t are distances between estimation location and observations, in space and time, respectively, and A_s and A_t are unit dependent, user defined weighting factors between separation distance in space vs. in time (how deep in space vs. time the sampling should occur). The unit dependent choice of A_s and A_t can be initially based on user expectations of the decorrelation distances in space vs. time and, if necessary, subsequently corrected accounting for actually computed decorrelation lengths in space and time in an iterative fashion. In this way temporal and spatial sampling depths could even be locally optimized and become location-specific. In the examples below (Section 3), A_s and A_t were set to 1 km^{-1}, and 0.5 day^{-1}, respectively, based on the observed average decorrelation distances in space and time (see Fig. 1 and Section 4.1).

[Figure 1]

h_s is calculated as the great circle distance between the centroid x_j of the estimation grid cell and the location x_i of an observation:

122
$$h_s(x_i, x_j) = r\cos^{-1}(\sin \varphi_i \sin \varphi_j + \cos \varphi_i \cos \varphi_j \cos(\lambda_i - \lambda_j)) \qquad (2)$$

123   where φ_i and λ_i are the latitude and longitude of location x_i and r is the radius of the Earth.

124   The temporal and spatial components of the probability function have different functional forms out of
125   necessity. The measurements often come pre-aggregated in time slices corresponding to hours, days, or
126   longer aggregation time periods, which multiplies the number of observations with the same time stamp.
127   As a result, it is not possible to assign sampling probability along a temporal axis in a manner equivalent to
128   the spatial approach; doing so would result in infinite probabilities assigned to all observations within the
129   time slice of the actual estimation location ($P_t \sim 1/0^2 = \infty$). The same holds for spatially co-located
130   observations. However, since each observation comes with unique spatial coordinates (not pre-binned like
131   in temporal case), we select a simpler form of the spatial component of the sampling function. The defined
132   form of P (Eq. 1) ensures that pairs of observations close to estimation location define the shape of the
133   variogram at short separation distances (the variogram should reflect variability in the spatio-temporal
134   vicinity of the estimation grid cell. See Section 2.2). Different forms of P can be used if directional
135   anisotropy is expected or if more/fewer observations along a given direction are desired to better represent
136   expected correlations.

137   Previous approaches required the user to choose spatial and temporal windows that determine which
138   neighboring observations to use (see, for comparison, Alkhaled et al. 2008; Hammerling et al. 2012a,b).
139   The approach proposed in this paper, by contrast, requires fewer subjective choices – only the form of
140   sampling function and unit dependent choice of normalizing coefficients A_s and A_t. In addition, our
141   approach is computationally feasible even for very large data sets.

2.2 Characterization of Spatio-temporal Covariance

143   Existing studies have used a number of models to estimate spatio-temporal covariances for a variety of
144   applications. Models used include the metric model (Dimitrakopoulos and Luo, 1994), linear model
145   (Rouhani and Hall, 1989), product model (De Cesare et al., 1996), non-separable model (Cressie and
146   Huang, 1999), and generalized product-sum covariance model (De Iaco et al., 2001). The approach
147   developed in this paper uses a generalized product-sum covariance model (De Iaco et al., 2001). This model
148   affords a number of advantages relative to other covariance models: (1) a product sum covariance model
149   outperformed other models in terms of prediction accuracy in a recent study using GOSAT satellite data
150   (Guo et al., 2013), (2) it is relatively easy to implement (De Iaco et al., 2001), and (3) it is more flexible
151   than a non-separable covariance model (De Cesare, 2001a).

152   The product-sum model, as it has been applied in the past, has one important area for improvement. The
153   original procedure (De Iaco et al., 2001) assumed separate modeling of the spatial and temporal covariance
154   (variograms) and their later unification into a spatio-temporal model in the final step. The procedure
155   requires observations approximately in the same location at multiple different times. However, satellite
156   observations are often not perfectly collocated in consequent measurement cycles over the same region. As
157   a result, we would need to assume that each measurement cycle is perfectly co-located with previous/future
158   cycles, or define an arbitrary tolerance, in order to apply the original approach. This assumption becomes
159   more prone to error if the observations are very sparse, as is often the case with satellites.

160   Thus, in this study, we cater to specific properties of satellite data and alter the original procedure by
161   estimating all covariance parameters simultaneously, thereby avoiding the aforementioned problem.

162   We broadly define the covariance as follows:

163
$$C_{s,t}(h_s,h_t) = \mathrm{Cov}(Z(s_+h_s,t_+h_t), Z(s,t)) \tag{3}$$

164 The equation shows that covariance between two points (Z) separated in space-time (s,t) depends on their
165 distance in space (h_s) and distance in time (h_t). The following class of valid product–sum covariance models
166 was introduced in De Cesare et al. (2001b) and further developed in De Iaco et al. (2001):

167
$$C_{s,t}(h_s,h_t)= k_1 C_s(h_s)C_t(h_t)+ k_2 C_s(h_s)+ k_3 C_t(h_t) \tag{4}$$

168 where C_t and C_s are valid temporal and spatial covariance models, respectively. De Iaco et al. (2001) proved
169 that for positive definiteness it is sufficient that $k_1 > 0$, $k_2 \geq 0$ and $k_3 \geq 0$. It is interesting to note that from
170 Eq. 4 follows that spatio-temporal covariance models collapses down to purely spatial model in cases where
171 temporal covariance does not exist. Thus, the spatial approach could be viewed as a special case of spatio-
172 temporal modeling.

173 The model in Eq. 4 corresponds to the spatio-temporal variogram shown in Equation 5. In the original
174 procedure, De Iaco et al., 2001 estimated separate spatial (h_t=0) and temporal (h_s=0) variograms using the
175 data. De Iaco et al., 2001 then combined these models to obtain the final spatio-temporal variogram model:

176
$$\gamma_{s,t}(h_s,h_t) = \gamma_{s,t}(h_s,0)+\gamma_{s,t}(0,h_t)-k\gamma_{s,t}(h_s,0)\gamma_{s,t}(0,h_t) \tag{5}$$

177 where $\gamma_{s,t}(h_s,0)$ and $\gamma_{s,t}(0,h_t)$ are spatio-temporal variograms for h_t=0 and h_s=0, respectively (Figure 2).
178 Parameter k is estimated from the data which makes the model easily applicable:

179
$$k = \frac{k_s C_s(0)+ k_t C_t(0)- C_{s,t}(0,0)}{k_s C_s(0)k_t C_t(0)} \tag{6}$$

180 where $k_s C_s(0)$ and $k_t C_t(0)$ are spatial and temporal sills (variances) obtained in modeling of separate
181 spatial and temporal variograms. The only condition k has to fulfill in order to create an admissible
182 covariance model is

183
$$0 < k \leq \frac{1}{max\{\sigma_s{}^2\left(\gamma_{s,t}(h_s,0)\right); \sigma_t{}^2\left(\gamma_{s,t}(0,h_t)\right)\}} \tag{7}$$

184 Due to the specifics of satellite data, we estimate both the covariance parameters and parameter k
185 simultaneously. This approach accounts for constraints that assure a positive definiteness of the model (De
186 Iaco et al., 2001). This simultaneous approach makes the model more applicable to sparse data and data
187 with variable spatial coverage, as is often the case with satellite observations.

188 We use a Gaussian variogram function with a nugget effect to model temporal covariance in the example
189 presented here (for an overview of variogram models see Chiles and Delfiner, 2012). We use an exponential
190 model for the spatial variogram. In both cases, we make this choice based upon visual inspection of local
191 variograms at multiple estimation locations:

192
$$\gamma_t(h_t)(Gaussian) = \begin{cases} 0, & for\ h_t = 0 \\ \sigma_t{}^2(1 - \exp\left(-\frac{h_t{}^2}{l_t{}^2}\right) + \sigma_{nug}^2, & for\ h_t > 0 \end{cases} \tag{8}$$

193
$$\gamma_s(h_s)(exponential) = \begin{cases} 0, & for\ h_s = 0 \\ \sigma_s{}^2(1 - \exp\left(-\frac{h_s}{l_s}\right) + \sigma_{nug}^2, & for\ h_s > 0 \end{cases} \tag{9}$$

194 where σ^2 and l are the variance and correlation length of the quantity being mapped, and σ^2_{nug} is the nugget
195 variance, typically representative of measurement and retrieval errors in the case of satellite observations.

196 [Figure 2]

197 Unlike the original procedure in De Iaco et al. (2001), we model the variogram using only two steps. First,
198 we calculate a raw spatio-temporal variogram based on the subsampled observations for each estimation
199 grid cell:

$$\gamma(h_s, h_t) = \tfrac{1}{2}[y(x_i) - y(x_j)]^2 \tag{10}$$

201 where γ is the raw spatio-temporal variogram value for a given pair of observations $y(x_i)$ and $y(\underline{x}_j)$, and h_s
202 and h_t are, respectively, the great circle distance and temporal distance between the spatio-temporal
203 locations (x_i and x_j) of these observations.

204 Second, we fit the theoretical variogram defined in Eq. 5 to the raw variogram using non-linear least
205 squares. We subsequently calculate the spatiotemporal covariance using the following equation:

$$C_{s,t}(h_s, h_t) = C_{s,t}(0,0) - \gamma_{s,t}(h_s, h_t)) \tag{11}$$

207 **Validity on the sphere.** Most covariance models were originally designed for Euclidean space, and their
208 validity in other coordinate systems cannot be assumed *per se*. Huang et al. (2011) examined the validity
209 of several theoretical covariance models in spherical coordinate systems. However, this evaluation has not
210 been done for the spatio-temporal product-sum covariance model. Other studies that use a product-sum
211 covariance model typically assume the validity of this covariance model on a sphere (e.g., Zeng et al., 2013;
212 Zeng et al., 2016). Results from Huang et al. (2011) explicitly validate the exponential covariance model
213 on a sphere, as well as sums of the products of exponential covariance models and constants (provided that
214 the constants are positive). The first term of the product-sum covariance model used in this study (Eq. 4)
215 represents a Hadamard product (Million, 2007) of two positive definite matrices. According to Schur
216 product theorem, a Hadamard product of two positive definite matrices necessarily gives a positive definite
217 matrix (Mathias, 1993). It therefore follows that a generalized product-sum model (Equation 4) is valid on
218 a sphere if its spatial component is valid on a sphere.

219 **2.3 Mapping using spatio-temporal moving window block kriging**

220 This section leverages the sampling function (Sect. 2.1) and the product-sum covariance model (Sect. 2.2)
221 to implement a spatio-temporal version of moving window block kriging. A primary advantage of block
222 kriging is its ability to estimate contiguous maps at any spatial resolution equal to or coarser than the spatial
223 support (i.e. footprint size) of observations (refer to Sect. 1 and Tadić et. al. 2015). Unlike ordinary kriging
224 method, the spatial support in block kriging corresponds to the average value within each chosen grid cell.

225 Moving window block kriging requires solving a set of linear equations to obtain a set of weights (λ). These
226 weights must be estimated for each prediction location using N associated observations:

$$\begin{bmatrix} \mathbf{Q} + \mathbf{R} & \mathbf{1} \\ \mathbf{1}^T & 0 \end{bmatrix} \begin{bmatrix} \lambda \\ -\nu \end{bmatrix} = \begin{bmatrix} \mathbf{q}_A \\ 1 \end{bmatrix} \tag{12}$$

228 In this equation, $\mathbf{R}$ is a diagonal $N{\times}N$ nugget covariance matrix that describes measurement and retrieval
229 errors, $\mathbf{Q}$ is a $N{\times}N$ covariance matrix among the N observations with individual entries as defined in Eqn.
230 11, $\mathbf{1}$ is an $N{\times}1$ unity vector, ν is a Lagrange multiplier, and $\mathbf{q}_A$ is an $N{\times}1$ vector of the spatio-temporal
231 covariances between the N observation locations and the estimation grid cell, defined as:

232
$$q_{A,i} = \frac{1}{n}\sum_{j=1}^{n} q\left(h_{s_{i,j}}, h_{t_{i,j}}\right) \tag{13}$$

233 where $q_{A,i}$ is the covariance between the grid cell and observation i. $q(h_{i,j})$ is defined as $C_{s,t}$ in Eqn. 11
234 based on the distances $h_{s_{i,j}}$ and $h_{t_{i,j}}$ between observation i and n regularly-spaced locations within the grid
235 cell. In the context of satellite measurements, n is a highest number of non-overlapping footprints contained
236 within a grid cell and was calculated based on the relative size of the satellite footprint compared to the
237 size of the estimation grid cells. n varies with latitude, as the size of grid cells decreases with the distance
238 from the equator. The system in Eqn. 12 is solved for the weights (λ) and the Lagrange multiplier (v). We
239 subsequently use these parameters to define the estimate ($\hat{z}$) and estimation uncertainty ($\sigma^2_{\hat{z}}$) for the grid
240 cell:

241
$$\hat{z} = \lambda^T \mathbf{y} \tag{14}$$

242
$$\sigma^2_{\hat{z}} = \sigma_{AA} - \lambda^T \mathbf{q}_A + v \tag{15}$$

243 where $\mathbf{y}$ is the $N \times 1$ vector of subsampled observations, and σ_{AA} is the variance of the observations at the
244 resolution of the estimation grid cell, defined as:

245
$$\sigma_{AA} = \frac{1}{n^2}\sum_{j=1}^{n}\sum_{k=1}^{n} q\left(h_{j,k}\right) \tag{16}$$

246 In that equation, $q\left(h_{s_{i,j}}, h_{t_{i,j}}\right)$ is defined as $C_{s,t}$ in Eqn. 11 based on the distances $h_{s_{i,j}}$ and $h_{t_{i,j}}$ between
247 any combination of the n regularly spaced locations within the grid cell defined previously.

248 # 3. Example applications

249 We select three case studies of satellite Level 2 data to demonstrate the properties of the method developed
250 in this paper: column-integrated dry air model fraction of CO_2 (XCO_2) from the Japanese Greenhouse Gas
251 Observing SATellite (GOSAT), CH_4 (XCH_4) from the Infrared Atmospheric Sounding Interferometer
252 (IASI), and solar-induced fluorescence (SIF) the Global Ozone Monitoring Experiment–2 (GOME-2).
253 Level 2 datasets from GOSAT, IASI and GOME-2 have relatively different characteristics. For example,
254 GOSAT observations are sparse while IASI and GOME-2 are abundant. These diverse datasets are therefore
255 ideal for testing the method developed here.

256 The method was demonstrated by producing two different sets of maps. First, it was applied at resolutions
257 coarser than native (1 × 1°, 2.5 × 2°, and 1 × 1° for GOSAT, IASI and GOME-2, respectively) to
258 demonstrate block kriging capabilities of the method (Section 3). Second, it was applied at the native
259 resolution of the satellites for cross-validation (method evaluation) purposes (Section 4).

260 ## 3.1 Total column CO_2 (XCO_2) observed by GOSAT

261 The Japanese Greenhouse Gas Observing SATellite (GOSAT) (e.g., Kuze et al., 2009), the first satellite
262 dedicated to global greenhouse gas monitoring, was launched in 2009. Basic information about the satellite,
263 its orbit configuration, and the CO_2 column observations are given in our previous study (Tadić et al., 2014).
264 It flies in a polar, sun-synchronous orbit with a 3-day repeat cycle and an approximate 13:00 LT overpass
265 time. GOSAT has a nadir footprint of about 10.5 km diameter at sea level (Kuze et al., 2009) and 2×10^3

266 observations per week. The XCO_2 observations from GOSAT have large retrieval uncertainties (e.g.,
267 O'Dell et al. 2012) and exhibit large spatial and temporal gaps (e.g., Fig. 3a). Although these XCO_2
268 observations are sparse and noisy, contiguous Level 3 maps are often desirable for environmental and
269 ecological applications (Maksyutov et al., 2013; Liu et al., 2012). To this end, we generate global daily
270 estimates for XCO_2 (August 2-7, 2009) to match the timeframe used in Tadić et al., 2014.

271 [Figure 3]

272 We obtain bias-corrected and filtered GOSAT Level 2 observations using NASA's Atmospheric CO_2
273 Observations from Space (ACOS) algorithm v3.4 release 3 (e.g., O'Dell et al., 2012; Crisp et al., 2012). In
274 this study, we use spatio-temporal moving window block kriging to create a series of contiguous, in-filled
275 global daily maps and associated uncertainties for 2-7 August 2009 (two repeat cycles) (Fig. 3a-c) at 1×1°
276 resolution. We select the time period to match the time period from our previous study (Tadić et al., 2014).
277 Unlike results from our previous study and other similar studies, which created estimates at 6-day or longer
278 time periods (Hammerling et al., 2012a), we leverage the method developed here to produce maps at the
279 daily scale.

3.2 Total column CH_4 (XCH_4) observed by IASI

281 The Infrared Atmospheric Sounding Interferometer (IASI) developed by the Centre National d'Etudes
282 Spatiales (CNES) in collaboration with the European Organisation for the Exploitation of Meteorological
283 Satellites (EUMETSAT) is a Fourier Transform Spectrometer based on a Michelson Interferometer coupled
284 to an integrated imaging system that measures infrared radiation emitted from the Earth. It is carried by
285 MetOp-A, a sun-synchronous polar orbit satellite which flows at an altitude of 817 km. Detailed information
286 about the IASI instrument could be found elsewhere (Crévoisier et al., 2009a,b; Massart et al., 2014). IASI
287 has an instantaneous field of view of 50×50 km, composed of four pixels each 12 km in radius, delivering
288 ~56×10^3 XCH_4 observations per week.

289 [Figure 4]

290 Methane Level 2 IASI (0-4 km) data were retrieved at the NOAA/NESDIS using the NUCAPS (NOAA
291 Unique CrIS/ATMS Processing System) algorithm (Gambacorta, 2013; Xiong et al., 2013). For the ice-
292 covered ocean the data for the lower troposphere (0-4 km) are unreliable due to insufficient thermal contrast
293 between the surface and the atmosphere. Filtering parameters have been provided by Xiong (2014, private
294 communication). The data are available at http://www.nsof.class.noaa.gov/. Using the new method, we
295 created a series of contiguous global daily maps and associated uncertainties for the Northern Hemisphere,
296 for February 26-March 4, 2013 (i.e. Figure 4a-c) at $1^o\times1^o$ resolution. We chose this time period to match
297 the occurrence of the methane "anomaly" North of the coast of Scandinavia.

3.3 Global land solar-induced fluorescence fields observed by GOME-2

299 The GOME-2 (The Global Ozone Monitoring Experiment–2) instrument on board METOP-A (e.g., Joiner
300 et al., 2013) observes solar-induced fluorescence (SIF). The GOME-2 spatial footprint (i.e. support) of the
301 observations is 40 km $\times$ 80 km (Joiner et al, 2013), and the volume of available data is approximately 2×10^5
302 SIF observations per week.

303   [Figure 5]

304   Multiple recent studies have demonstrated the potential use of satellite observations of solar-induced
305   fluorescence (SIF) for understanding the photosynthetic CO_2 uptake at large scales (Joiner et al., 2011;
306   Joiner et al., 2012; Joiner et al., 2013; Frankenberg et al., 2011; Frankenberg et al., 2012; Guanter et al.,
307   2012, Lee et al., 2013; Frankenberg et al., 2014). Satellite SIF measurements can be used with land surface
308   models to understand GPP response to environmental stress (e.g., Lee et al., 2013) and to improve the
309   representation of GPP. GOME-2 provides the highest spatial and temporal density of data, among all
310   available datasets.

311   In the example presented here we use SIF GOME-2 v.14 data (Joiner et al., 2013) with the approach
312   described in Section 2 to create contiguous maps of SIF at a single spatial resolution ($1^\circ \times 1^\circ$) and daily
313   temporal resolutions. Maps of SIF and associated uncertainties are created at daily temporal resolutions
314   covering 5-14 May, 2012, some of which are shown on Figures 5a-c.

315   ## 4. Method evaluation: accuracy, precision and bias

316   ### 4.1 Accuracy, precision and bias

317   We use a leave-one-out cross validation technique to assess the performance of spatio-temporal (ST) versus
318   spatial moving window block kriging. We produce these estimates at the native resolution of GOSAT, IASI
319   and GOME-2 satellites/instruments, which allowed a direct comparison to measured values. For IASI and
320   GOME-2, for each day in February 26-March 4, 2013, and May 5-14, 2012, respectively, 10% of available
321   observational data were randomly selected for use in leave-one-out cross-validation and their coordinates
322   extracted. For XCO_2, all GOSAT XCO_2 observations for each day in August 2-7, 2009, were used. We
323   assess the accuracy (the difference between estimates and withheld observations) of both methods using
324   two common measures: (1) Mean Absolute Error (MAE), and (2) Root Mean Squared Error (RMSE). We
325   also use two more recently proposed measures (Li and Heap, 2011; Li, 2016) that remove the effect of
326   unit/scal. The first is relative mean absolute error (RMAE) that is given as:

327

328     $$\text{RMAE} = \frac{1}{n}\sum_{i=1}^{n}|(\hat{z}_i - y_i)/o_i| \times 100 \qquad (17)$$

329

330   and the second is relative root mean square error (RRMSE), as follows:

331

332     $$\text{RRMSE} = \left[\frac{1}{n}\sum_{i=1}^{n}(|y_i - \hat{z}_i|/y_i)^2\right]^{1/2} \times 100 \qquad (18)$$

333   where n is the number of observations or samples, o is observed value, and p is predicted or estimated value.

334   We assess the performance of each method using two additional measures: (3) the accuracy of the
335   uncertainty bounds (the degree to which the reported uncertainties capture the difference between estimates
336   and withheld observations) and (4) bias (the mean difference between estimates and withheld observations).

337   We parameterize the temporal component of the spatio-temporal sampling function in such a way
338   that observations located +/- 3 days from the actual date had 10% probability of being sampled

339 compared to observations from the actual day (see Fig 1a). We compare the results to spatial
340 kriging estimates obtained in two different ways, based on observations only from the actual day
341 (1d) and based on observations from +/-3 days from the actual day (7d). This latter case is
342 analogous to the +/- 3-day window that we use for the ST approach. In this 7d case, we obtain
343 these spatial kriging results by assuming the entire observational dataset collected within the
344 selected time period (actual day +/- 3 days) is perfectly temporally correlated. In other words, we
345 use all observations as though they were collected at the same time. We then produce estimates at
346 locations of observations collected within the selected timeframe and compare the performance of
347 the two methods. We repeat procedure described in Section 2 for every observation selected for
348 cross-validation, and we average the statistics, displayed in Table 1.

349 [Table 1]

350 According to the results, the spatio-temporal approach performs better than the spatial (7d) approach in all
351 three cases and in all performance measures (for example, spatial (7d) MAE was 6-10% larger). The
352 comparison clearly shows that proper characterization of the temporal covariance between two points
353 residing in different time periods (days), embedded into spatio-temporal approach, improves kriging
354 performance. In IASI and GOME-2 cases, the spatio-temporal method also performed better than spatial
355 (1d). However, in case of GOSAT data, spatio-temporal approach slightly underperformed the spatial (1d)
356 approach having 12% higher MAE (please see Section 4.2 for discussion).

357 We observed that RMAE and RRMSE error measures should be used with caution in cases when
358 observations can take real zero values, like in the GOME-2 case. In such cases the division by close-to-zero
359 values result in extremely high RMAE and RRMSE values, which overall limits the applicability of these
360 error measures.

361 We evaluate the accuracy of the uncertainty bounds by examining how often those bounds encapsulate
362 withheld observations. The percentage of observations that fall outside the uncertainty bounds in spatio-
363 temporal approach is comparable to that of the spatial method, confirming the accuracy of the estimated
364 uncertainty bounds (for normally-distributed data the percentage of observations that fall outside of the one,
365 two, and three estimations standard deviation ($\sigma_{\hat{z}}$) uncertainty bounds should be 32%, 5% and 0.3%,
366 respectively). The fraction of observations that fall outside the uncertainty bound is generally lower than
367 would be expected for normally-distributed data, and our results may indicate non-normal features in the
368 data.

4.2 When is spatio-temporal modeling recommended?

370 A ST approach can afford advantages over purely spatial methods when temporal data correlations and data
371 coverage are strong. Indeed, in many cases, the ST approach is more accurate than a purely spatial method
372 (Table 1). This result is consistent with existing literature which uniformly reports that ST approaches are
373 more accurate than spatial approaches (Zeng et al., 2013; Guo et al., 2013; Zeng et al., 2016).

374 However, although considering information from days preceding and following the target estimation day
375 should in principle always provide a further constraint on the estimate, this does not guarantee that an ST
376 method will always outperform a spatial-only method in practice. The prime reasons for this are two-fold.
377 First, because computational limitations cap the number of observations that can be considered, considering
378 observations across multiple days necessarily leads to a reduction in the spatial density of observations

379 being considered. This first factor can be partially alleviated by carefully designing the selection probability
380 function (Eqn. 1). The second reason is that implementing a ST approach involves the estimation of a larger
381 number of covariance parameters (Eqn. 4-9) relative to a spatial-only approach, which can introduce
382 additional uncertainty. Indeed, we observe that the purely spatial approach performs better than the ST
383 method in some cases (e.g., the GOSAT case).

384 Overall, a ST approach is likely to outperform a spatial-only approach when the data exhibit one (or more)
385 of three characteristics. First, a ST approach is likely better when the data are sparse or unequally
386 distributed. In these cases, a ST approach can intelligently leverage data in adjacent time periods to
387 compensate for the sparsity of data in the time period of interest. Second, an ST approach works well for
388 datasets with temporal gaps (e.g., due to cloud cover or instrument malfunction). An ST approach can fill
389 these gaps while a spatial-only approach cannot be used for temporal gap-filling. Third, an ST-approach is
390 well-suited to datasets with regional biases that manifest in one time slice but that do not repeat in adjacent
391 time slices. The difference between the performance of ST and S-approaches obtained through cross-
392 validation becomes most pronounced in processing datasets with measurement errors that are spatially but
393 not temporally correlated. In these cases, an ST approach can use data from adjacent time periods to obtain
394 an estimate, data that do not have the same regional, spatially-correlated biases. Although the resulting
395 estimate may appear inferior during cross-validation, this is because that estimate will not reproduce
396 regional biases in data from the time slice of interest. A spatial-only approach, by contrast, will reproduce
397 these regional biases because it does not use data from adjacent times when creating the estimate. As a
398 result, a spatial-only approach will appear to perform better in cross validation, but the ST approach will
399 more accurately reflect the true, underlying process.

5. Conclusions

401 In this study, we develop a method to create high spatio-temporal resolution maps from satellite data using
402 spatio-temporal moving window block kriging based on product-sum covariance model. The method relies
403 on a limited number of assumptions: that the observed physical quantity is spatio-temporally auto-
404 correlated, and that its nature can be inferred from the observations.

405 The method has several advantages over previously applied methods. Apart from the advances alluded to
406 in Sect. 1: 1) it improves covariance parameters estimation procedure because it does not model spatial and
407 temporal covariance separately, 2) it allows for great flexibility in the choice of sampling function and 3) it
408 provides estimates even for the time periods when measurements are not available. It can exploit
409 correlations with both past and future periods of the observed time spot to provide the most accurate
410 estimates.

411 We demonstrate the applicability of this method by creating Level 3 products from the GOSAT XCO_2, IASI
412 CH_4 and GOME-2 SIF data. Sparse XCO_2 observations from GOSAT and dense XCH_4 and SIF
413 observations from IASI and GOME-2 make a perfect test ground for the method. We show that the proposed
414 method can even map XCO_2 on daily time scales. The method generally yields more precise and accurate
415 (and unbiased) estimates compared to spatial method which used the same observations but assumed perfect
416 temporal correlation between data. The factors which could affect the performance of the ST method are
417 discussed in Section 4.2.

418 This approach could be used in the future to produce real-time estimates not only of XCO_2, XCH_4 or SIF,
419 but of other environmental data observed by satellites which exhibit spatio-temporal autocorrelations.
420 Especially important could be satellite datasets that have spatially, but not temporally, correlated errors. In

421 such cases, sampling across several time periods could perhaps help isolate and remove them, which should
422 be a subject of further studies.

423 The method could be applied in a standalone mode or as part of a broader satellite data processing package.
424 Maps produced by the spatio-temporal approach could then be incorporated into physical and
425 biogeochemical models of the Earth system.

6. Code availability

427 The documented Matlab source code is available at the Researchgate website
428 (https://www.researchgate.net/publication/311595272_Spatio-
429 temporal_approach_to_moving_window_block_kriging_of_satellite_data_v10_code; DOI:
430 10.13140/RG.2.2.21411.04643).

Acknowledgement

432 This work was supported by the National Aeronautics and Space Administration (NASA) through grant no.
433 NNX12AB90G and NNX13AC48G, and the National Science Foundation (NSF) through grant no.
434 1342076. Satellite CH_4 IASI v5 data are supplied by the NOAA National Environmental Satellite, Data,
435 and Information Service (NESDIS): http://www.nsof.class.noaa.gov/. We would also like to thank Leonid
436 Yurganov (JCET) and Nathaniel Lebedda (University of Maryland) for helpful information and discussions.

References

438 Chiles, J.-P. and Delfiner, P.: Geostatistics, second edition, Wiley, 2012.

439 Cressie, N. and Huang, H. C.: Classes of nonseperable, spatio-temporal stationary covariance functions,
440 Journal of the American Statistical Association, 94, 1 – 53, 1999.

441 Crévoisier, C., Nobileau, D., Fiore, A. M., Armante, R., Chédin, A., and Scott, N. A.: Tropospheric
442 methane in the tropics – first year from IASI hyperspectral infrared observations, Atmos. Chem. Phys., 9,
443 6337–6350, doi:10.5194/acp-9-6337-2009, 2009a.

444 Crévoisier, C., Chédin, A., Matsueda, H., Machida, T., Armante, R.,and Scott, N. A.: First year of upper
445 tropospheric integrated content of CO_2 from IASI hyperspectral infrared observations, Atmos. Chem. Phys.,
446 9, 4797–4810, doi:10.5194/acp-9-4797-2009, 2009b.

447 Crisp, D., Fisher, B. M., O'Dell, C., Frankenberg, C., Basilio, R., Bösch, H., Brown, L. R., Castano, R.,
448 Connor, B., Deutscher, N. M., Eldering, A., Griffith, D., Gunson, M., Kuze, A., Man10 drake, L., McDuffie,
449 J., Messerschmidt, J., Miller, C. E., Morino, I., Natraj, V., Notholt, J., O'Brien, D. M., Oyafuso, F.,
450 Polonsky, I., Robinson, J., Salawitch, R., Sherlock, V., Smyth, M., Suto, H., Taylor, T. E., Thompson, D.
451 R., Wennberg, P. O., Wunch, D., and Yung, Y. L.: The ACOS CO_2 retrieval algorithm – Part II: Global
452 XCO_2 data characterization, Atmos. Meas. Tech., 5, 687–707, doi:10.5194/amt-5-687-2012, 2012.

453 De Cesare, L., Myers, D. E., and Posa, D.: Spatio-temporal modelling of SO_2 in Milan district. In: Baafi,
454 E. Y., Schofield, N. A. (Eds.), Geostatistics Wollongong. Kluwer Academic Publishing, Dordrecht, pp.
455 1031 – 1042, 1996.

456   De Cesare, L., Myers, D. E., and Posa, D.: Product–sum covariance for space–time modeling: an
457   environmental application. Environmetrics 12, 11 – 23, 2001a.

458   De Cesare, L., Myers, D., and Posa, D.: Estimating and modeling space–time correlation structures: Stat.
459   Prob. Lett., v. 51, no. 1, 9–14, 2001b.

460   Dimitrakopoulos, R., and Luo, X.: Spatiotemporal Modeling: Covariances and Ordinary Kriging Systems,
461   Geostatistics for the Next Century, Kluwer Academic Publishers, Dordrecht, 88-93, 1994.

462   Frankenberg, C., Fisher, J. B., Worden, J., Badgley, G., Saatchi, S. S., Lee, J.-E., Toon, G. C., Butz, A.,
463   Jung, M., Kuze, A., and Yokota, T.: New global observations of the terrestrial carbon cycle from GOSAT:
464   Patterns of plant fluorescence with gross primary productivity, Geophys. Res. Lett., 38, L17706,
465   doi:10.1029/2011GL048738, 2011.

466   Frankenberg C, O'Dell C, Guanter L, McDue J.: Remote sensing of near-infrared chlorophyll fluorescence
467   from space in scattering atmospheres: implications for its retrieval and interferences with atmospheric CO2
468   retrievals. Meas. Tech. 5, 2081–2094., doi:10.5194/amt-5-2081-2012, 2012.

469   Frankenberg, C., O'Dell, C., Berry, J., Guanter, L., Joiner, J., Köhler, P., et al.: Prospects for chlorophyll
470   fluorescence remote sensing from the Orbiting Carbon Observatory-2, Remote Sensing of Environment,
471   147, 1-12, doi: 10.1016/j.rse.2014.02.007, 2014.

472   Gambacorta A.: The NOAA Unique CrIS/ATMS Processing System (NUCAPS): Algorithm Theoretical
473   Basis Documentation, NOAA Center for Weather and Climate Prediction (NCWCP), Version 1.0, August
474   21, 2013, http://www.star.nesdis.noaa.gov/jpss/documents/ATBD/NUCAPS_ATBD_20130821.pdf

475   Guanter, L., Frankenberg, C., Dudhia, A., Lewis, P. E., Gomez-Dans, J., Kuze, A., Suto, H., and Grainger,
476   R. G.: Retrieval and global assessment of terrestrial chlorophyll fluorescence from GOSAT space
477   measurements, Remote Sens. Environ., 121, 236– 251, doi:10.1016/j.rse.2012.02.006, 2012.

478   Guo, L., Lei, L. and Zeng, Z.: Spatiotemporal correlation analysis of satellite-observed CO_2: Case studies
479   in China and USA. Geoscience and Remote Sensing Symposium (IGARSS), 2013 IEEE International, 21-
480   26 July, Melbourne, VIC, 2013.

481   Hammerling, D. M., Michalak, A. M., and Kawa, S. R.: Mapping of CO_2 at high spatiotemporal resolution
482   using satellite observations: Global distributions from OCO-2, J. Geophys. Res., 117, D06306,
483   doi:10.1029/2011JD017015, 2012a.

484   Hammerling, D. M., Michalak, A. M. O'Dell, C., and Kawa, S. R.: Global CO_2 distributions over land from
485   the Greenhouse Gases Observing Satellite (GOSAT), Geophysical Research Letters, 39, L08804,
486   doi:10.1029/2012GL051203, 2012b.

487   Huang, C., Zhang, H., and Robeson, S. M.: On the validity of commonly used covariance and variogram
488   functions on the sphere, Math. Geosci., 43, MR2824128, 721–733, doi: 10.1007/s11004-011-9344-7, 2011.

489   De Iaco, S., Myers, D., and Posa, D.: Space-time analysis using a general product–sum model: Stat. Probab.
490   Lett., v. 52, no. 1, 21–28, 2001.

491   Joiner, J., Yoshida, Y., Vasilkov, A. P., Yoshida, Y., Corp, L. A., and Middleton, E. M.: First observations
492   of global and seasonal terrestrial chlorophyll fluorescence from space, Biogeosciences, 8, 637-651,
493   doi:10.5194/bg-8-637-2011, 2011.

Joiner, J., Yoshida, Y., Vasilkov, A. P., Middleton, E. M., Campbell, P. K. E., Yoshida, Y., Kuze, A., and Corp, L. A.: Filling-in of near-infrared solar lines by terrestrial fluorescence and other geophysical effects: simulations and space-based observations from SCIAMACHY and GOSAT, Atmos. Meas. Tech., 5, 809–829, doi:10.5194/amt-5-809-2012, 2012.

Joiner, J., Guanter, L., Lindstrot, R., Voigt, M., Vasilkov, A. P., Middleton, E. M., Huemmrich, K. F., Yoshida, Y., and Frankenberg, C.: Global monitoring of terrestrial chlorophyll fluorescence from moderate spectral resolution near-infrared satellite measurements: methodology, simulations, and application to GOME-2, Atmos. Meas. Tech., 6, 2803-2823, doi:10.5194/amt-6-2803-2013, 2013.

Liu, J., Fung, I., Kalnay, E., Kang, J.-S., Olsen, E. T., and Chen, L.: Simultaneous assimilation of AIRS Xco2 and meteorological observations in a carbon climate model with an ensemble Kalman filter, J. Geophys. Res., 117, D05309,doi:10.1029/2011JD016642, 2012.

Matthias, K., and Cressie, N.: Spatio-temporal smoothing and EM estimation for massive remote-sensing data sets, Journal of Time Series Analysis 32.4, 430-446, doi: 10.1111/j.1467-9892.2011.00732.x, 2011.

Katzfuss, M. and Cressie, N.: Bayesian hierarchical spatio-temporal smoothing for very large datasets. Environmetrics, 23: 94–107. doi: 10.1002/env.1147, 2012.

Kuze, A., Suto, H., Nakajima, M., and Hamazaki, T.: Thermal and near infrared sensor for carbon observation Fourier-transform spectrometer on the Greenhouse Gases 5 Observing Satellite for greenhouse gases monitoring, Appl. Optics, 48, 6716–6733, doi:10.1364/AO.48.006716, 2009.

Lee, J.-E., Frankenberg, C., van der Tol, C., Berry, J. A., Guanter, L., Boyce, C. K., Fisher, J. B., Morrow, E., Worden, J. R., Asefi, S., Badgley, G., and Saatchi S.: Forest productivity and water stress in Amazonia: observations from GOSAT chlorophyll fluorescence Proc. R. Soc. B, 280(1762), doi: 10.1098/rspb.2013.0171, 2013.

Li, J., and Heap, A.D.: Spatial interpolation methods applied in the environmental sciences: a review. Environ. Model. Softw. 53, 173–189, doi: http://dx.doi.org/10.1016/j.envsoft.2013.12.008, 2014.

Li, J. and Heap, A.: A review of comparative studies of spatial interpolation methods in environmental sciences: performance and impact factors. Ecol. Inf. 6, 228e241, 2011.

Li, J.: Assessing spatial predictive models in the environmental sciences: Accuracy measures, data variation and variance explained, Environmental Modelling & Software, Volume 80, Pages 1-8, ISSN 1364-8152, http://dx.doi.org/10.1016/j.envsoft.2016.02.004, 2016.

Maksyutov, S., Takagi, H., Valsala, V. K., Saito, M., Oda, T., Saeki, T., Belikov, D. A., Saito, R., Ito, A., Yoshida, Y., Morino, I., Uchino, O., Andres, R. J., and Yokota, T.: Regional CO_2 flux estimates for 2009–2010 based on GOSAT and ground-based CO2 observations, Atmos. Chem. Phys., 13, 9351–9373, doi:10.5194/acp-13-9351-2013, 2013.

Mathias, R.: Matrix completions, norms and Hadamard products, Proc. Amer. Math. Soc. 117 (4), 905–918, 1993.

Million, E.: The Hadamard Product. http://buzzard.ups.edu/courses/2007spring/projects/million-paper.pdf, 2007. Accessed on 15 January 2015.

531 NASA Earth Science: http://science.nasa.gov/earth-science/earth-science-data/data-processing-levels-for-
532 eosdis-data-products/, last access: 23 July, 2014.

533 Nguyen, H., Katzfuss, M., Cressie, N. and Braverman, A.: Spatio-Temporal Data Fusion for Very Large
534 Remote Sensing Datasets, Technometrics, Vol. 56, Iss. 2, doi: 10.1080/00401706.2013.831774, 2014.

535 O'Dell, C. W., Connor, B., Bösch, H., O'Brien, D., Frankenberg, C., Castano, R., Christi, M., Eldering, D.,
536 Fisher, B., Gunson, M., McDuffie, J., Miller, C. E., Natraj, V., Oyafuso, F., Polon15 sky, I., Smyth, M.,
537 Taylor, T., Toon, G. C., Wennberg, P. O., and Wunch, D.: The ACOS CO_2 retrieval algorithm – Part 1:
538 Description and validation against synthetic observations, Atmos. Meas. Tech., 5, 99–121,
539 doi:10.5194/amt-5-99-2012, 2012.

540 Rouhani, S., and Hall, T.J.: Space-Time Kriging of Groundwater Data. In: Armstrong, M. (Ed.),
541 Geostatistics. Kluwer Academic Publishers, Dordrecht, Vol. 2, 639-651, 1989.

542 Tadić, J., Qiu, X., Yadav, V. and Michalak, A.: Mapping of satellite Earth observations using moving
543 window block kriging, Geosci. Model Dev., 8, 1–9, doi:10.5194/gmd-8-1-2015, 2015.

544 Xiong X., Barnet C., Maddy E., Gambacorta A., King T., and Wofsy S.: Mid-upper tropospheric methane
545 retrieval from IASI and its validation. Atmos Meas Tech. 6: 2255-2265, 2013.

546 Zeng, Z., LiPing, L., L. LiJie, G., Li, Z., Bing, Z.,: Incorporating temporal variability to improve
547 geostatistical analysis of satellite-observed CO_2 in China, Chinese Science Bulletin, 58(16), 1948-1954,
548 2013.

549 Zeng, Z., Lei, L., Strong, K., Jones, D. B. A., Guo, L., Liu, ., Deng, F., Deutscher, N. M., Dubey, M. K.,
550 Griffith, D. W. T., Hase, F., Henderson, B., Kivi, R., Lindenmaier, R., Morino, I., Notholt, J., Ohyama,H.,
551 Petri, C., Sussmann, R., Velazco, V., A., Wennberg, P., O., and Lin, H.: Global land mapping of satellite-
552 observed CO_2 total columns using spatio-temporal geostatistics, International Journal of Digital Earth, DOI:
553 10.1080/17538947.2016.1156777, 2016.

554

555

556

557

558 **Table 1**. Cross-validation results of GOSAT XCO_2, IASI XCH_4 and GOME-2 SIF datasets using spatio-
559 temporal and spatial methods, including mean absolute error (MAE), root mean squared error (RMSE),
560 relative mean absolute error (RMAE), relative root mean square error (RRMSE), percent of observations
561 lying outside of one, two, and three standard deviations ($\sigma_{\hat{z}}$) of the mapping uncertainty, and mean
562 difference. MAE, RMSE and bias units for GOSAT, IASI and GOME-2 are ppm, ppb and $mW/m^2/sr/nm$,
563 respectively. RMAE and RRMSE are unitless, and due to the reasons explained in Section 4.1 given only
564 for GOSAT and IASI. Shaded fields represent best estimate in each category for every satellite.

	GOSAT XCO$_2$	IASI XCH$_4$	GOME-2 SIF

		ST	1d	7d	ST	1d	7d	ST	1d	7d
Estimates	Mean absolute error (MAE)	0.83	0.74	0.89	19.19	20.23	21.04	0.52	0.54	0.54
	Root mean squared error (RMSE)	1.12	0.98	1.21	25.25	27.10	27.77	0.68	0.69	0.69
	Relative mean absolute error (RMAE)	0.22	0.19	0.23	1.04	1.09	1.14	-	-	-
	Relative root mean square error (RRMSE)	0.29	0.25	0.31	1.37	1.46	1.50	-	-	-
Uncertainties	% observations falling outside $1\sigma_2$ uncertainty	9.13	15.03	10.70	11.02	9.06	13.84	14.60	12.14	24.80
	% observations falling outside $2\sigma_2$ uncertainty	1.12	3.01	1.39	0.48	0.51	0.86	1.20	0.64	4.33
	% observations falling outside $3\sigma_2$ uncertainty	0.067	0.52	0.13	0.04	0.046	0.022	0.11	0.05	0.83
Bias	Mean difference	-0.012	0.0066	-0.034	0.28	-0.14	0.58	0.016	0.0013	0.032

565

566

567
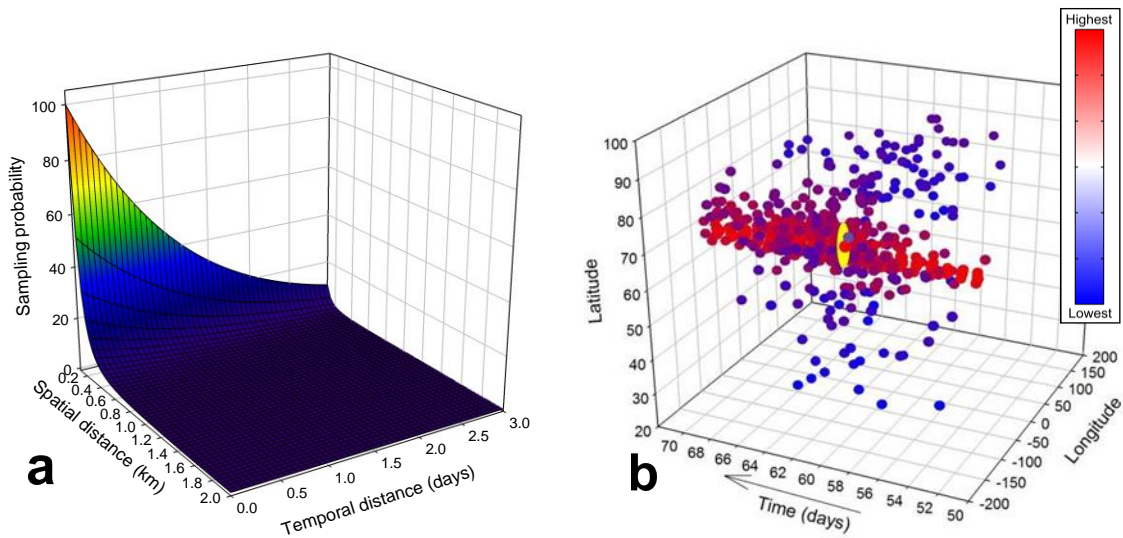
568

569   **Figure 1**. (a) Sampling probability as a decreasing function of spatial and temporal distance as used in this
570   study, (b) The typical example of subsampled IASI Level 2 XCH_4 (altitude below 4 km) data for a selected
571   estimation location (yellow circle). Color of observations shows semivariance between observation and
572   estimation location (blue-lowest, red-highest). Due to stronger temporal covariance, the relative decrease
573   of the sampling probability along temporal axis is smaller than with spatial distance.

574

575
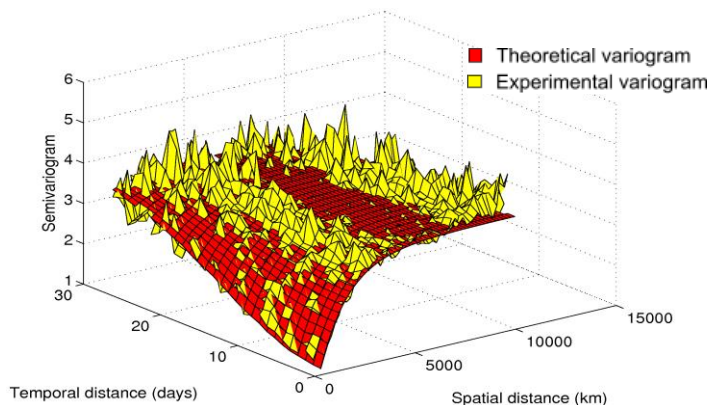
576

577   **Figure 2.** Illustration of experimental and fitted theoretical spatio-temporal variogram for GOSAT XCO_2
578   data.

579
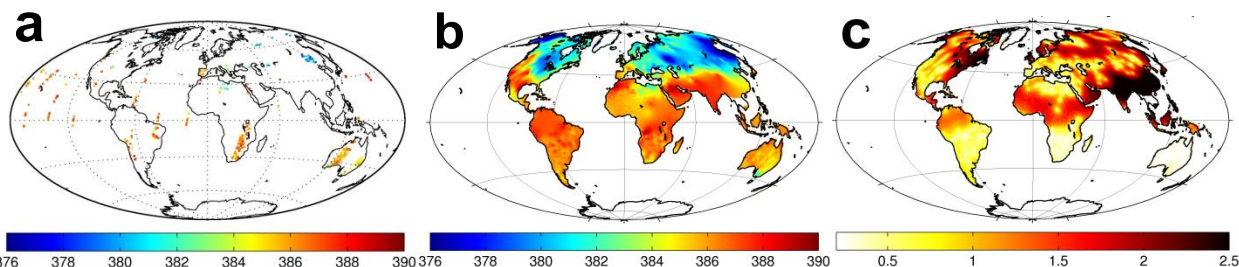
580

581   **Figure 3.** (a) GOSAT/ACOS v3.4 XCO_2 retrievals (Level 2 data) (ppm) for August 3, 2009 (b) Contiguous
582   global GOSAT/ACOS v3.4 maps (Level 3 data) (ppm) for the same day obtained using Spatio-temporal
583   Moving Window Block Kriging at $1 \times 1°$ spatial resolution, (c) associated uncertainties, given as 1-sigma
584   ($\sigma_{\hat{z}}$) (ppm).

585

586
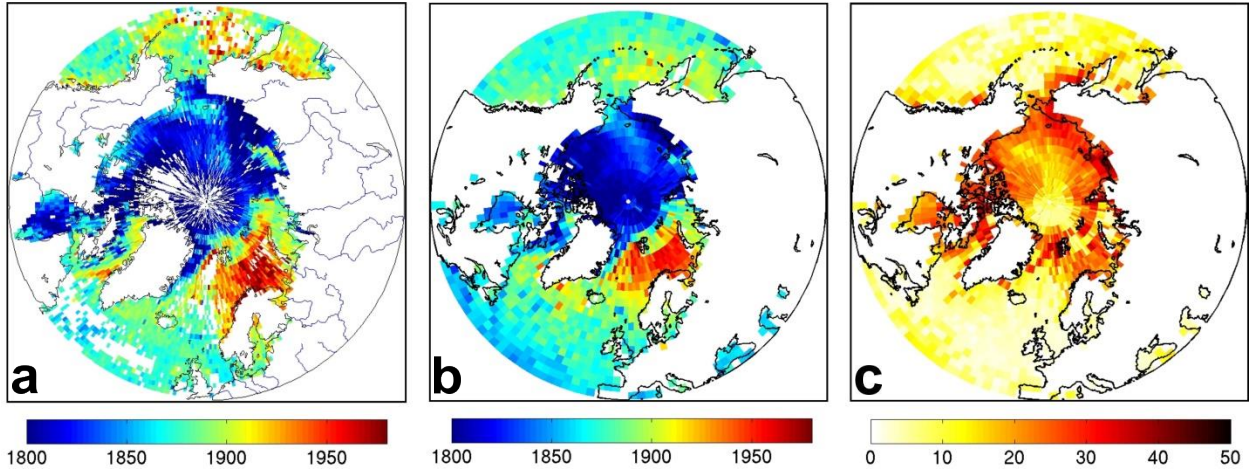
Figure 4. (a) IASI XCH$_4$ (0-4 km) retrievals (ppb) for March 2, 2013 (sea only), (b) Contiguous IASI maps for Northern Hemisphere for the same day obtained using Spatio-temporal Moving Window Block Kriging at $2.5 \times 2°$ spatial resolution and (c) associated uncertainties, given as 1-sigma ($\sigma_{\hat{z}}$) (ppb).
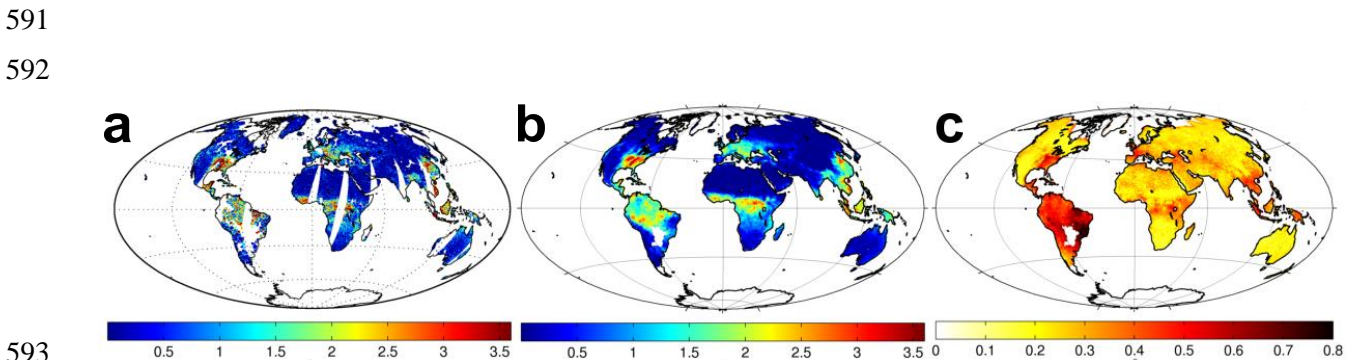
Figure 5. (a) GOME-2 SIF v14 retrievals (Level 2 data) (mW/m^2/sr/nm) for May 5, 2012, (b) Contiguous global GOME-2/SIF v14 maps (Level 3 data) (mW/m^2/sr/nm) for the same day obtained using Spatio-temporal Moving Window Block Kriging at $1 \times 1°$ spatial resolution, (c) associated uncertainties, given as 1-sigma ($\sigma_{\hat{z}}$) (mW/m^2/sr/nm).